







UNIVERSIDAD DISTRITAL
FRANCISCO JOSÉ DE CALDAS



Research

Numerical Study on the Structural Behavior of the Blade Profile of a Savonius-Type Rotor while Implementing a Multiblade Geometry

Estudio numérico del comportamiento estructural del perfil del álabo de un rotor tipo Savonius implementando una geometría multielemento

Luis A. Gallo¹  , Edwin L. Chica¹ , and Elkin G. Flórez² 

¹Universidad de Antioquia (Medellin, Colombia).

²Universidad de Pamplona (Pamplona, Colombia).

Abstract

Context: This study evaluates the structural stability of a Savonius-type rotor by implementing a multiblade profile, with the purpose of reducing the resistance to movement and consequently improving aerodynamic performance. The rotor with the profile under study was compared against rotors with conventional semicircular and split Bach profiles.

Method: The fluid-structure interaction was analyzed by numerically simulating the three rotors, and the state of stresses and deformations was determined under a normal operating regime. The rotors were assigned the same construction material, and they were studied under the same parameters and models of fluid dynamics and computational mechanics via the ANSYS software.

Results: The results obtained showed a better structural behavior in the rotor with the multiblade configuration, reducing the maximum equivalent stress by 59,10 and 42,87% and the deformations by 47,40 and 33,59% with respect to the rotors with the conventional semicircular and split Bach profiles, respectively.

Conclusions: The multiblade configuration allows for greater aerodynamic and structural performance while preserving the construction and operation simplicity that characterize Savonius-type rotors.

Keywords: CFD, multiblade, multiphysics, Savonius rotor, wind energy.

Article history

Received:
08th/Mar/2022

Modified:
05th/Oct/2022


Accepted:
16nd/Nov/2022

Ing., vol. 28, no. 2,
2023. e19174

©The authors;
reproduction right
holder Universidad
Distrital Francisco
José de Caldas.

Open access



*  **Correspondence:** luis.gallo@udea.edu.co

Resumen

Contexto: Este estudio evalúa la estabilidad estructural de un rotor tipo Savonius implementando un perfil multielemento, con el propósito de reducir la resistencia al movimiento y mejorar así el rendimiento aerodinámico. El rotor con el perfil en estudio se comparó con rotores de perfiles semicircular convencional y Bach dividido.

Método: Se analizó la interacción fluido-estructura mediante la simulación numérica de los tres rotores, y se determinó el estado de esfuerzos y deformaciones en un régimen normal de operación. A los rotores se les asignó el mismo material de construcción, y estos fueron estudiados bajo los mismos parámetros y modelos de la dinámica de fluidos y mecánica computacional a través del software ANSYS.

Resultados: Los resultados obtenidos evidenciaron un mejor comportamiento estructural en el rotor con la configuración multielemento, al reducir el esfuerzo equivalente máximo en 59,10 y 42,87 % y las deformaciones en 47,40 y 33,59 % con respecto a los rotores de perfiles semicircular convencional y Bach dividido respectivamente.

Conclusiones: La configuración multielemento permite un mayor rendimiento aerodinámico y estructural, a la vez que se conserva la simplicidad de construcción y operacional que caracterizan al rotor tipo Savonius.

Palabras clave: CFD, energía eólica, multielemento, multifísica, rotor Savonius.

| | | | |
|--|-------------|--|-----------|
| Table of contents | | 3.1. Results analysis | 9 |
| | Page | 4. Discussion | 10 |
| 1. Introduction | 2 | 5. Conclusions | 13 |
| 2. Materials and methods | 3 | 6. Acknowledgments | 14 |
| 2.1. Geometrical details of the rotors . . | 3 | 7. Author contributions | 14 |
| 2.2. Numerical analysis | 4 | References | 14 |
| 3. Results | 9 | | |

1. Introduction

The omnidirectional functioning of vertical-axis wind turbines (VAWTs) allows them to take advantage of winds with variable direction without requiring additional orientation systems (1–3). Likewise, in the last few years, it has been proven that VAWTs can operate at a shorter distance between rotors than horizontal-axis wind turbines (HAWTs), which allows for a greater number of turbines available in the same area (4,5).

The Savonius-type VAWT, whose operation principle is mainly based on aerodynamic drag force, has a high initial torque and can be operated at a low flow velocity without the need for assistance

devices to start its movement (6–9). However, this type of operation requires a blade that moves against the flow when returning to its working position, generating an opposite torque. This significantly reduces its performance, and it is mainly because of this that this type of rotor barely reaches values close to 50 % the performance of HAWTs (7, 10–12).

In previous studies, it was evidenced that employing multiblade profiles in the blades of this type of rotors can improve their performance by 10,8 % with respect to a profile without the secondary element (split Bach profile), as well as by 51,2 % regarding conventional semicircular profiles (Fig. 1) (6, 13–17). Additionally, the implementation of a multiblade geometry allows greatly preserving the construction and operation simplicity that characterize Savonius-type rotors (13).

After determining that a rotor with a multiblade Bach profile has a higher aerodynamic efficiency with respect to the conventional semicircular and split Bach profiles, it was also necessary to compare its structural behavior before aerodynamic loads. Therefore, this study aimed to assess the structural stability of a Savonius-type rotor while implementing a multiblade profile. The maximum equivalent stress (Von Mises tension) (18–21) and the maximum deformation were determined as contrast variables, which were obtained through computational simulations of the rotor models' structural behavior (22–24).

2. Materials and methods

2.1. Geometrical details of the rotors

Tridimensional models 200 mm in diameter (D) and 300 mm in height (H) were established for the three profiles, consisting of three stages with an offset of 120° in the azimuth angle (25). Discs with a diameter of 220 mm were installed in the ends of each stage (26). The blades were built considering 1 mm wall thickness and 2 mm thickness for the discs that separate each stage (Fig. 1).

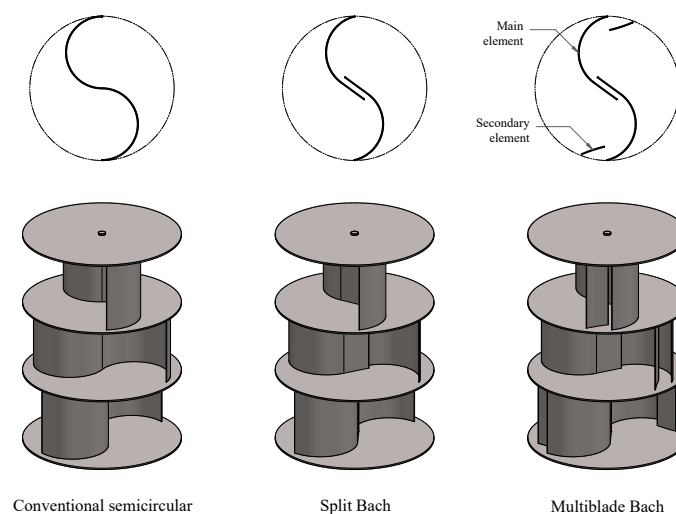


Figure 1. Rotor models analyzed in this study and their corresponding blade profiles

These measurements were established with the purpose to seek dimensional correspondence with the numerical studies of the profiles (13, 14), as well as to implement an aspect relation in accordance with that recommended in literature ($AR = H/D = 1,5$) (27). A multistage configuration was considered, as it allows analyzing the profile in different azimuth positions and reducing the fluctuation of the load (28). Thus, it is possible to reduce the deviation between a static analysis with lower computational costs and a dynamic one that generally demands more solver resources.

The geometrical properties for each profile are detailed in Table I.

Table I. Geometrical properties for each profile

| Property | Conventional semicircular | Split Bach | Multiblade Bach |
|--|---------------------------|--------------------|--------------------|
| Profile length [mm] | 313,59 | 314,14 | 380,23 |
| Cross-sectional area (A_o) [mm ²] | 313,37 | 313,72 | 379,37 |
| Second moment of area about x (I_x) [mm ⁴] | $1,41 \times 10^6$ | $1,12 \times 10^6$ | $1,51 \times 10^6$ |
| Second moment of area about y (I_y) [mm ⁴] | $1,49 \times 10^5$ | $8,58 \times 10^4$ | $2,08 \times 10^5$ |
| Second polar moment of area (I_z) [mm ⁴] | $1,56 \times 10^6$ | $1,21 \times 10^6$ | $1,72 \times 10^6$ |

The second moments of area can be expressed through Eq. (1), where the averaged second moment of area in the xy plane is constant in any azimuth position (23, 24). Likewise, I_z can be used as the characteristic dimension of the second moment of area (Fig. 2).

$$I_z = I_x + I_y \quad (1)$$

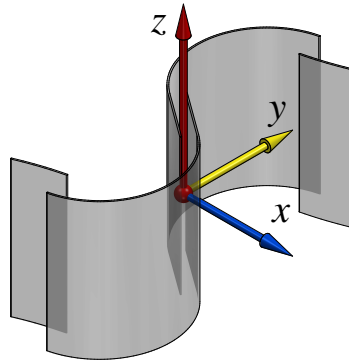


Figure 2. Reference system used to determine the second moments of area

2.2. Numerical analysis

This study was carried out through the multiphysical analysis of a two-way fluid-structure interaction, which allows for feedback between the results of each of the physics involved, linking tools of computational fluid dynamics (CFD) with those of computational solid mechanics (CSM) (29–34).

The three geometries were studied in a steady state, employing the same CFD and CSM algorithms, parameters, and models via the ANSYS Fluent and Mechanical solvers, which solve the physics of each phenomenon through the finite volume and the finite element methods, respectively (35–41).

The ANSYS Workbench automatically exchanges data between simulation solvers. Its mesh mapping technology ensures that data are transferred more accurately from CFD analysis to CSM and *vice versa* (Fig. 3).

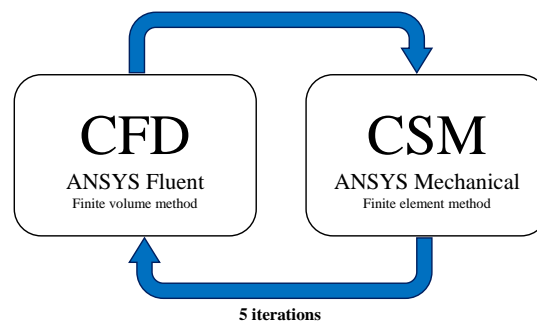


Figure 3. Two-way fluid-structure interaction for the study case

This coupling considers the pressure field of the fluid dynamic analysis and the consequences of this load in the structural analysis. A limit of five calculation cycles or iterations in the two-way coupling was established.

A turbulence model $k - \omega SST$ was proposed due to its good performance in predicting free and adverse pressure gradient flows (42–44). The convergence criterion for the solution residuals was fixed in the order of 10^{-3} .

The domain of analysis comprises two bodies: a fluid body and a solid body. The fluid body is made up of two parts: an orthohedral region that simulates the far fluid field, and a cylindrical one for the near fluid field, which contains the geometry of the rotor.

An air inlet was established at a velocity of $v = 4 \text{ m/s}$ (wind class 1) (45), corresponding to a flow regime with a Reynolds number of 6×10^4 . Likewise, the outlet was fixed at atmospheric conditions, and the side field was simulated under symmetry conditions, since it is there that low-scale gradients occur (42, 46).

The rotor walls rotate at a fixed angular velocity $\omega = 20 \text{ rad/s}$, corresponding to a $TSR = 0,5$, in whose proximity the greatest torque load occurs (Fig. 4) (13).

The speed ratio at the tip of the blade (TSR) gives a proportion of the angular velocity of the rotor in dimensionless terms, according to Eq. (2).

$$TSR = \frac{\omega D}{2v} \quad (2)$$

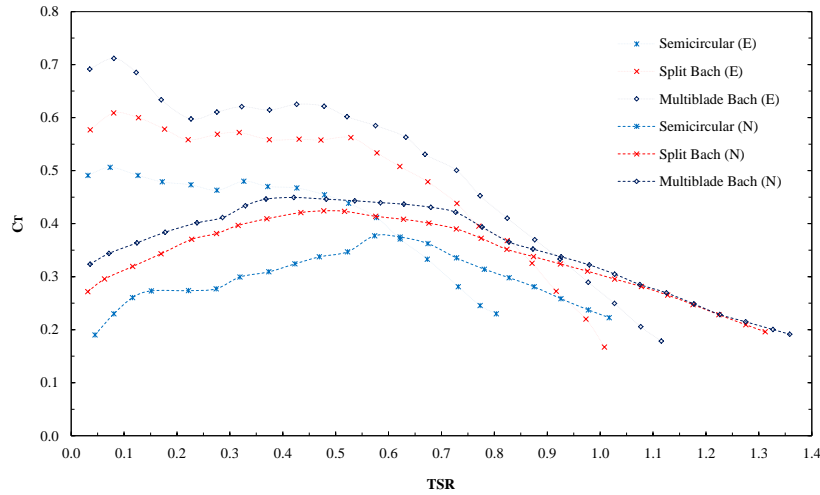


Figure 4. Experimentally obtained C_T results by the three tested rotors (E) and their comparison with the numerical results determined from the three-dimensional simulations (N)

Source: (13)

The torque coefficient (C_T) is estimated as the ratio between the torque generated by the rotor on its shaft (T) and the torque that is possible to generate under the given conditions (47,48). This is expressed by Eq. (3), where ρ is the density of the air and $A = DH$ is the frontal area of the rotor.

$$C_T = \frac{T_{turbine}}{T_{available}} = \frac{T}{\frac{1}{4} \rho A v^2 D} \tag{3}$$

The dimensions of the computational domain were set as follows: 10 m wide, 1 m high, and 10 m long, seeking to reduce the blockage effect caused by the rotor in the flow section (Fig. 5) (49,50).

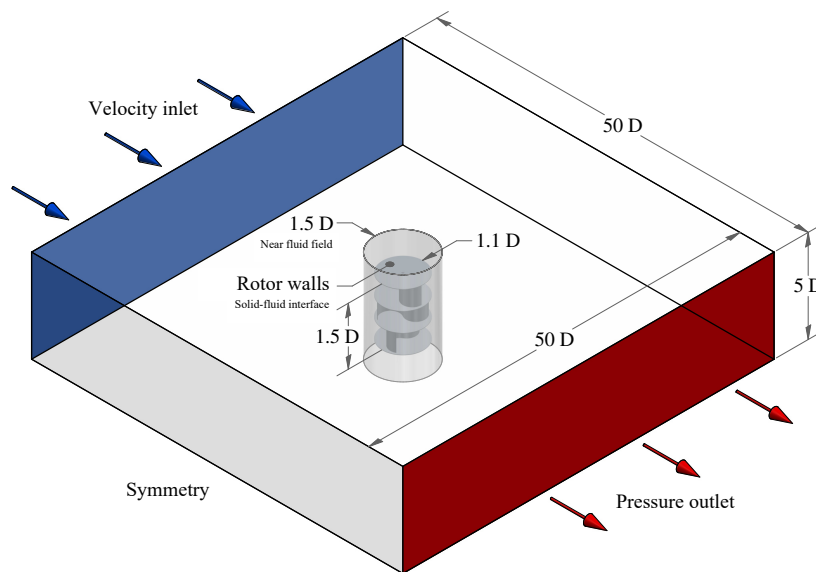


Figure 5. Three-dimensional analysis domain and its boundary conditions

In order to obtain an efficient number of partitions into which the analyzed domain had to be divided, it was necessary to carry out an independence analysis for spatial discretization, seeking to obtain convergence in the result. The rotor with the conventional semicircular profile was used as a test model during the independence analysis.

Since the model was made up of two bodies, an independence analysis was carried out for each of them. For the fluid body, five discretizations (known as *meshing*) were built with the same structure, but with an increased number of partitions in each edge according to the refinement of each mesh. The region that simulated the far field of the fluid had a structured mesh with only hexahedral elements (Figs. 6a and 6b), while the region that simulated the fluid field near the rotor had an unstructured mesh with only tetrahedral elements in order to gain greater adaptability to the geometry (Figs. 6c and 6d). The meshing adjacent to the rotor walls was refined and had a structure of perpendicular layer (*inflation*) that allowed for a better prediction of the boundary layer (Fig. 6e).

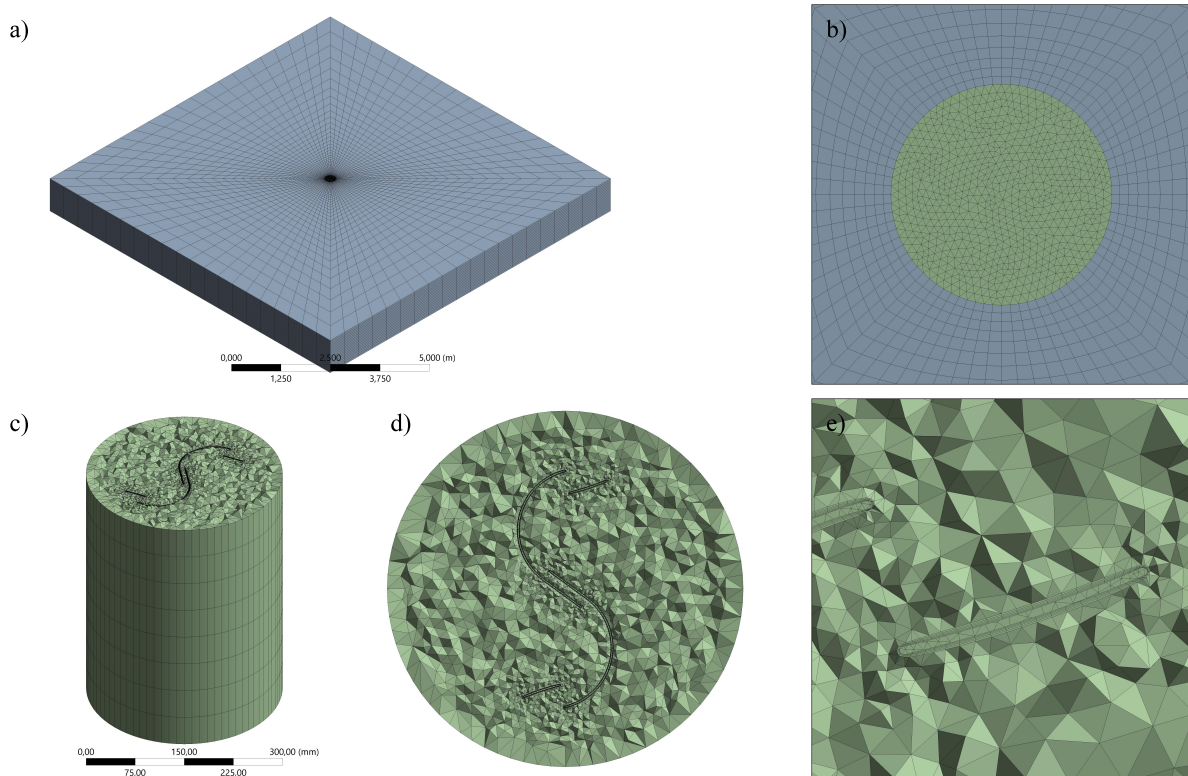


Figure 6. General structure of the meshing for the CFD analysis of the multiblade Bach rotor: (a) region far field of the fluid, (b) detail of the transition from the far field to the near field of the fluid, (c) cutaway view of region near field of the fluid, (d) profile geometry detail, and (e) detail of the profile walls

In the same way, for the solid body that simulated the rotor, five meshings were built, which were defined by predominant hexahedral elements forming structured faces on the walls of the blades (Fig. 7).

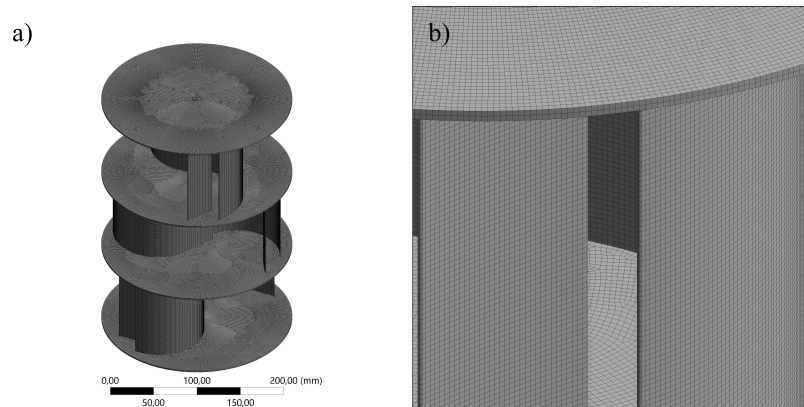


Figure 7. General structure of the meshing for the CSM analysis of the multiblade Bach rotor: (a) isometric view of the rotor model and (b) detail of the model walls

When solving each case with the different meshings, the maximum equivalent stress value was obtained, whose variation was observed to become smaller as the meshing became finer (Tables II and III). For fluid and solid body analysis, the asymptotic convergence indicators, according to the Richardson extrapolation, were 1,0042 and 1,0289, respectively, whose closeness to the unit indicates the existence of a convergence value (51).

For the meshing of the fluid body, the value of y^+ was also analyzed, which is recommended to be lower than the unit when using the turbulence model $k - \omega SST$, thus ensuring appropriate predictions in the flow near the walls (42). In this way, the third meshing was selected for both the fluid and the solid bodies.

Table II. Mesh independence test results for the fluid body

| Meshing | 1 | 2 | 3 | 4 | 5 |
|---------------------------------|---------|---------|-----------|-----------|------------|
| Number of elements | 119.791 | 478.077 | 1.805.411 | 7.473.517 | 30.180.988 |
| Maximum equivalent stress [MPa] | 0,29665 | 0,30367 | 0,30768 | 0,30867 | 0,30897 |
| Deviation | 3,89 % | 1,67 % | 0,41 % | 0,09 % | |
| y^+ | 5,21 | 2,56 | 0,96 | 0,54 | 0,42 |
| Simulation time [hours] | 3,62 | 4,24 | 7,23 | 23,36 | 92,65 |

Table III. Mesh independence test results for the solid body

| Meshing | 1 | 2 | 3 | 4 | 5 |
|---------------------------------|---------|---------|---------|-----------|------------|
| Number of elements | 59.641 | 238.166 | 912.667 | 3.750.668 | 15.102.672 |
| Maximum equivalent stress [MPa] | 0,22798 | 0,28475 | 0,30768 | 0,31307 | 0,31656 |
| Deviation | 27,98 % | 10,05 % | 2,81 % | 1,10 % | |
| Simulation time [hours] | 0,45 | 1,81 | 7,23 | 29,12 | 122,45 |

The supports and the loads of the model were considered as shown in Fig. 8. A fixed support was located in the lower hub of the rotor, simulating a full load exerted by the generator. Similarly, a cylindrical support was placed on the upper hub, simulating the restriction in the bearing. Additionally, the aerodynamic loads imported from the fluid dynamic analysis were applied to the rotor surface.

In this analysis, the loads on the rotor body (weight and centripetal force) were not taken into account, since they are not linearly scalable, given their dependence on the mass, so the result could not be generalized ($mass \propto scale^3$).

Polyethylene was defined as the construction material, as it is a commonly used medium-strength polymer. Table IV shows its main structural properties.

Table IV. Established properties for polyethylene as a construction material

| Property | Magnitude |
|---------------------------|--------------|
| Density | 950 kg/m^3 |
| Poisson ratio | 0,42 |
| Elasticity module | 1100 MPa |
| Yield strength | 25 MPa |
| Ultimate tensile strength | 33 MPa |

B: Static Structural
Static Structural
Time: 1, s

- A** Cylindrical Support: 0, mm
- B** Fluid Solid Interface
- C** Fixed Support

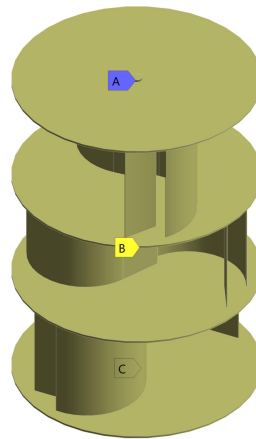


Figure 8. Established supports and loads for the multiblade Bach rotor model

3. Results

3.1. Results analysis

After solving the fluid physics, each rotor's states of pressure and flow velocity were obtained. Fig. 9 shows the state of static pressure exerted by the fluid on the walls of the multiblade Bach rotor

model by means of a contour graph. In the same figure, the fluid path lines and the corresponding velocity magnitude are shown for a flow plane. Areas of laminar flow, stagnation, recirculation, and fluid acceleration can be identified.

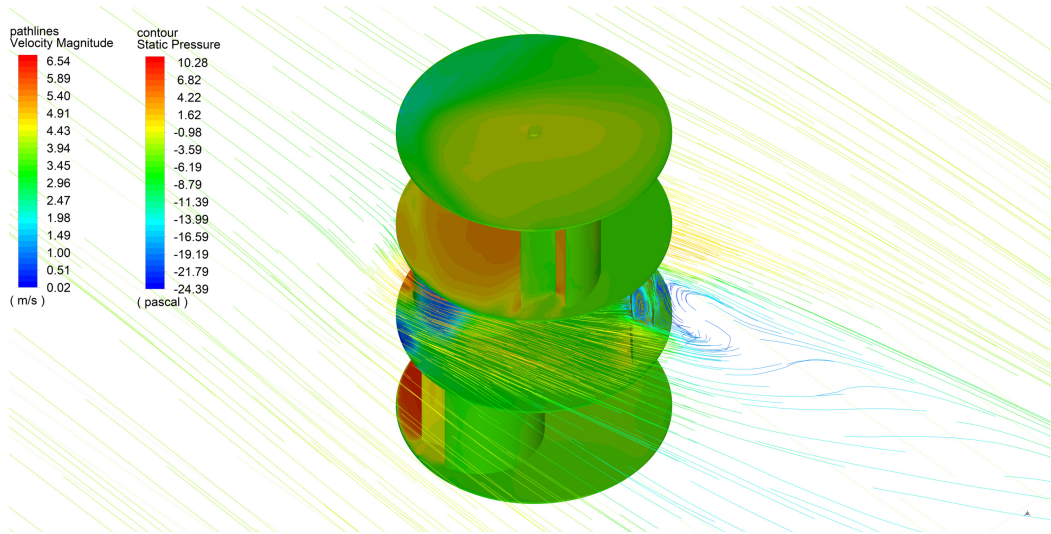


Figure 9. Results of the fluid dynamics on the multiblade Bach rotor for a wind of 4 m/s and a TSR of 0,5

After transferring the result of the fluid dynamics analysis to the structural one, the stress and deformation states for each rotor were obtained, whose maximum values are summarized in Table V. Fig. 10 shows, represented by contours, an example of the multiblade Bach rotor's state of stress and deformation.

Table V. Structural analysis results

| Rotor model | Conventional semicircular | Split Bach | Multiblade Bach |
|--|---------------------------|------------|-----------------|
| Aerodynamic load (F) [N] | 0,46085 | 0,48876 | 0,53771 |
| Torque load (T) [$N \cdot m$] | 0,01213 | 0,01728 | 0,01748 |
| Maximum equivalent stress (σ) [MPa] | 0,30768 | 0,33277 | 0,21157 |
| Maximum deformation (δ) [mm] | 0,15034 | 0,17989 | 0,13296 |

4. Discussion

As seen in Table V, the aerodynamic loads exerted on the rotor models vary as a result of the different profile shapes. These differences in loading conditions hinder a direct comparison of the structural results.

Because the generated torque is a consequence of the aerodynamic load, it is necessary to obtain a static equivalence that explains its origin, as each profile has different capabilities when it comes

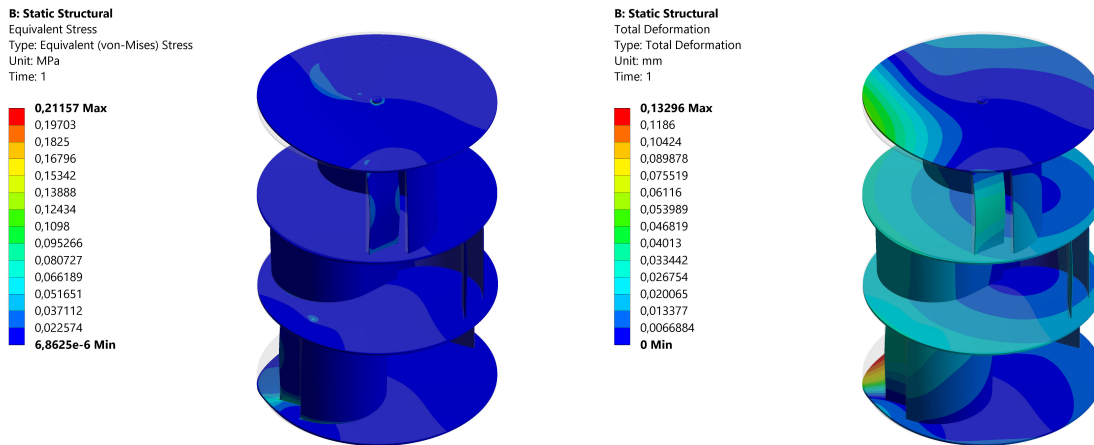


Figure 10. State of equivalent stress (left) and total deformation (right) of the multiblade Bach rotor for a wind of 4 m/s and a TSR of $0,5$

to converting this aerodynamic load into useful torque. Likewise, these differences in torque induce variations in the stress and strain state of the rotor.

Eq. (4) describes the equivalent percentage of the aerodynamic load, which, when applied to the blade tip, is responsible for the generated torque, with e_{load} being the load effectiveness.

$$e_{load} = \frac{2T}{FD} \times 100\% \quad (4)$$

In the same way, when comparing the second polar moment of area with the maximum moment that can be obtained with the same area, the effectiveness in the distribution of the profile area with regard to the rigidity of the structure can be explained. Eq. (5) allows obtaining the maximum second polar moment of area given the cross-sectional area and the diameter. Likewise, Eq. (6) shows this relationship, where e_{area} is the area effectiveness.

$$I_{z_{max}} = \frac{A_o D^2}{4} - \frac{A_o^2}{2\pi} \quad (5)$$

$$e_{area} = \frac{I_z}{I_{z_{max}}} \times 100\% \quad (6)$$

By determining the ratio for each rotor model, the values plotted in Fig. 11 are obtained. It can be seen that the conventional semicircular profile has the least load effectiveness, *i.e.*, it generates great aerodynamic resistance while delivering low torque. In contrast, the split Bach profile offers the greatest load effectiveness, allowing a higher torque to be achieved with less resistance. Although the load effectiveness of the multiblade Bach profile is between that of the two previous profiles, its value is greater than the average of the two. This shows that the aerodynamic load exerted on the multiblade Bach rotor is the highest, as a consequence of a greater power transmission.

On the other hand, the greatest area effectiveness is reported by the conventional semicircular profile, which shows a greater concentration of area in the outermost region of the geometry of the profile. In contrast, the least area effectiveness is observed in the split Bach profile, indicating that the

area is more concentrated towards the center of the geometry. Although the area effectiveness of the multiblade Bach profile is between that of the two previous profiles, its value is greater than the average of the two.

Both indicators were multiplied to obtain a structural effectiveness value which showed that the changes made to the geometries, starting from the conventional semicircular profile, had positive impacts on structural stability. An increasing trend in the evolution of the rotor can be seen by means of this indicator.

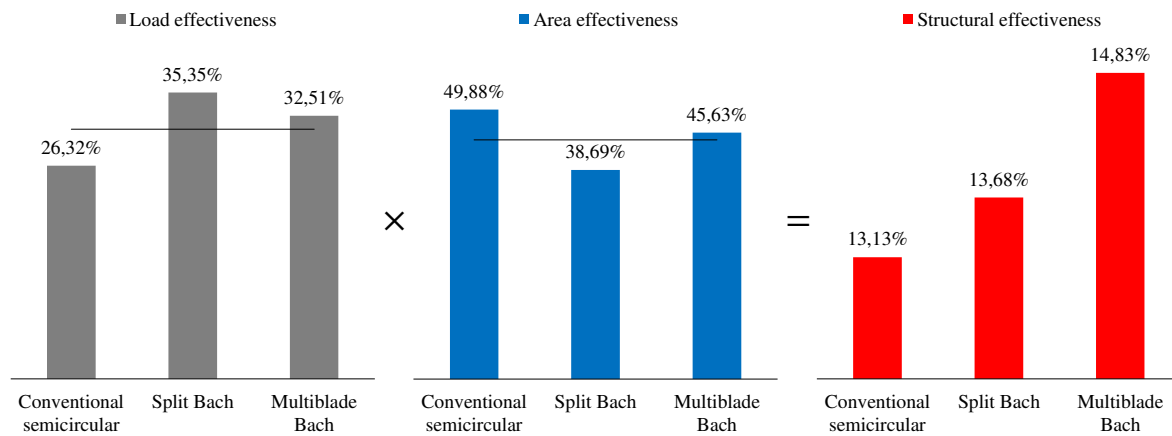


Figure 11. Load (left), area (center), and structural (right) effectiveness in profile geometries. Black lines represent the average effectiveness for the conventional semicircular and split Bach profiles.

Considering that the stresses and deformations (σ , δ) are directly proportional to the loads (F , T) (23, 24), it is possible to adjust the results of the conventional semicircular and split Bach rotors to the loading conditions of the multiblade Bach. To this effect, the compound proportionality method described in Eq. (7) is implemented.

$$\sigma_{adj_i} = \sigma_i \frac{F_j}{F_i} \frac{T_j}{T_i} \quad \delta_{adj_i} = \delta_i \frac{F_j}{F_i} \frac{T_j}{T_i} \quad (7)$$

where the subscripts adj , i , and j refer to the adjusted value, rotor i , and rotor j (multiblade Bach rotor in this case), respectively. Thus, the values reported in Table V were adjusted under the same load conditions of the multiblade Bach profile and are presented in Fig. 12.

The results in Fig. 12 reveal a consistent trend with the structural effectiveness results (Fig. 11), with the values of the adjusted maximum equivalent stress and deformation being significantly lower for the multiblade geometry, which indicates that the multiblade Bach profile offers greater strength and stiffness.

The adjusted maximum equivalent stresses were reduced by 59,10 and 42,87%, and the deformations by 47,40 and 33,59% with respect to the conventional semicircular and split Bach profiles, respectively.

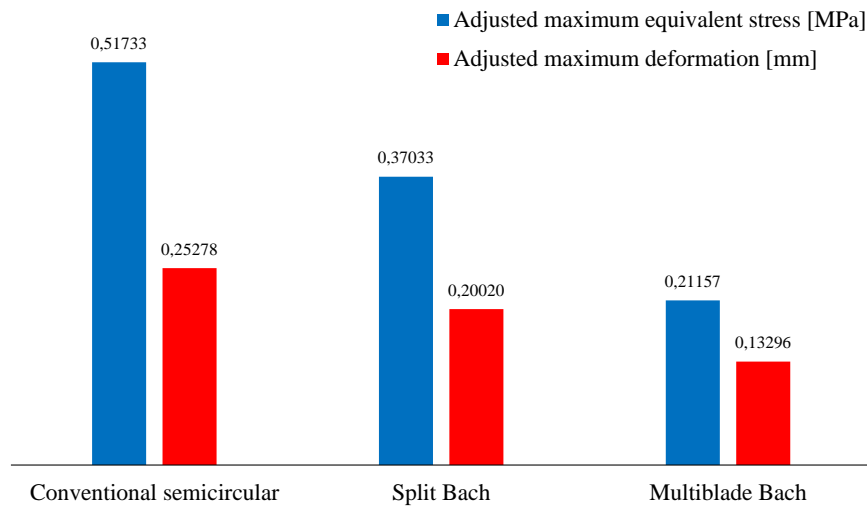


Figure 12. Adjusted maximum equivalent stress and deformation for each rotor

This additional structural stability is provided by the greater moment of area provided by the secondary element of the multiblade profile, where the I_z of the multiblade Bach profile is 42,47% greater than that of the split Bach.

The mass moment of inertia (I_M) is directly proportional to the second polar moment of area, with the constant of proportionality being the product between the density of the construction material (ρ_M) and the height of the blade, as described in Eq. (8).

$$I_M = \rho_M H \cdot I_z \quad (8)$$

Therefore, as the second polar moment of area increases, the mass moment of inertia also increases. This means a greater difficulty for the rotor to start its movement. However, in the case of the multiblade profile, this is compensated by the higher static torque that is generated when the rotor starts up (Fig. 4) (13). Additionally, a greater inertia reduces the fluctuation of the torque transmitted, working as a flywheel.

5. Conclusions

This study compared the structural behavior under aerodynamic loads of rotors with conventional semicircular, split Bach, and Bach multiblade profiles. The models were studied via a two-way fluid-structural interaction analysis and in a steady state.

The results revealed that the multielement rotor had greater strength and stiffness, provided by the increase in the second polar moment of area implied by the secondary element in the profile. The maximum equivalent stresses were reduced by 59,10 and 42,87%, and the deformations by 47,40 and 33,59% with regard to the conventional semicircular and split Bach profiles, respectively.

The implementation of the secondary element allows for a greater aerodynamic and structural performance, preserving, to a large extent, the construction and operation simplicity that characterizes Savonius-type rotors, requiring an addition of only 21 % of the material involved for manufacturing the main elements.

6. Acknowledgments

The authors gratefully acknowledge the financial support provided by the Colombia Scientific Program within the framework of call Ecosistema Científico [contract number FP44842-218-2018].

7. Author contributions

Luis A. Gallo: Conceptualization, Investigation, Methodology, Software, Writing – original draft.

Edwin L. Chica: Writing – review & editing, Data curation, Supervision, Resources

Elkin G. Flórez: Project administration, Supervision, Resources

References

- [1] A. A. Mohammed, H. M. Ouakad, A. Z. Sahin, and H. Bahaidarah, "Vertical axis wind turbine aerodynamics: Summary and review of momentum models," *J. Energy Resour. Technol.*, vol. 141, no. 5, 2019. <https://doi.org/10.1115/1.4042643>. ↑ 2
- [2] S. Eriksson, H. Bernhoff, and M. Leijon, "Evaluation of different turbine concepts for wind power," *Renew. Sust. Energ. Rev.*, vol. 12, no. 5, pp. 1419–1434, 2008. <https://doi.org/10.1016/j.rser.2006.05.017>. ↑ 2
- [3] K. Ibrahim, V. S. Djanali, and N. Ikhwan, "Numerical study of bach-bladed savonius wind turbine with varying blade shape factor," *JMES Int. J. Mech. Sci.*, vol. 4, no. 2, pp. 12–21, 2020. <http://dx.doi.org/10.12962/j25807471.v4i2.7839>. ↑ 2
- [4] B. Zhang, B. Song, Z. Mao, and W. Tian, "A novel wake energy reuse method to optimize the layout for Savonius-type vertical axis wind turbines," *Energy*, vol. 121, pp. 341–355, 2017. <https://doi.org/10.1016/j.energy.2017.01.004>. ↑ 2
- [5] J. T. Hansen, M. Mahak, and I. Tzanakis, "Numerical modelling and optimization of vertical axis wind turbine pairs: A scale up approach," *Renew. Energ.*, vol. 171, pp. 1371–1381, 2021. <https://doi.org/10.1016/j.renene.2021.03.001>. ↑ 2
- [6] S. J. Savonius, "The S-rotor and its applications," *Mech Eng.*, vol. 53, no. 5, pp. 333–338, 1931. ↑ 3
- [7] L. Chen, J. Chen, and Z. Zhang, "Review of the Savonius rotor's blade profile and its performance," *Renew. Sust. Energ. Rev.*, vol. 10, no. 1, p. 013306, 2018. <https://doi.org/10.1063/1.5012024>. ↑ 3
- [8] K. Golecha, M. Kamoji, S. Kedare, and S. Prabhu, "Review on Savonius rotor for harnessing wind energy," *Wind. Eng.*, vol. 36, no. 6, pp. 605–645, 2012. <https://doi.org/10.1260/0309-524X.36.6.605>. ↑ 3

- [9] A. Kumar and R. P. Saini, "Performance parameters of Savonius type hydrokinetic turbine: A review," *Renew. Sust. Energ. Rev.*, vol. 64, pp. 289–310, 2016. <https://doi.org/10.1016/j.rser.2016.06.005>. ↑ 3
- [10] S. J. Savonius, "Vertical axis wind turbine," 1929. US Patent 1,697,574. ↑ 3
- [11] H. H. Al-Kayiem, B. A. Bhayo, and M. Assadi, "Comparative critique on the design parameters and their effect on the performance of S-rotors," *Renew. Energ.*, vol. 99, pp. 1306–1317, 2016. <https://doi.org/10.1016/j.renene.2016.07.015>. ↑ 3
- [12] Y. Cengel and J. Cimbala, *Fluid Mechanics: Fundamentals and Applications, Forth Edition*. New York: McGraw-Hill Education, 2018. ↑ 3
- [13] L. A. Gallo, E. L. Chica, E. G. Flórez, and F. A. Obando, "Numerical and experimental study of the blade profile of a Savonius type rotor implementing a multi-blade geometry," *Appl. Sci.*, vol. 11, no. 22, p. 10580, 2021. <https://doi.org/10.3390/app112210580>. ↑ 3, 4, 5, 6, 13
- [14] L. A. Gallo, E. L. Chica, and E. G. Flórez, "Numerical optimization of the blade profile of a savonius type rotor using the response surface methodology," *Sustainability*, vol. 14, no. 9, p. 5596, 2022. <https://doi.org/10.3390/su14095596>. ↑ 3, 4
- [15] S. Roy and U. K. Saha, "Wind tunnel experiments of a newly developed two-bladed Savonius-style wind turbine," *Appl. Energy*, vol. 137, pp. 117–125, 2015. <https://doi.org/10.1016/j.apenergy.2014.10.022>. ↑ 3
- [16] J. V. Akwa, G. A. da Silva Júnior, and A. P. Petry, "Discussion on the verification of the overlap ratio influence on performance coefficients of a Savonius wind rotor using computational fluid dynamics," *Renew. Energ.*, vol. 38, no. 1, pp. 141–149, 2012. <https://doi.org/10.1016/j.renene.2011.07.013>. ↑ 3
- [17] L. A. Gallo, E. L. Chica, and E. G. Flórez, "Estudio de desempeño de distintos perfiles de álabes de una turbina eólica para aprovechar vientos de baja velocidad," *Ing.*, vol. 27, no. 1, 2022. <https://doi.org/10.14483/23448393.18127>. ↑ 3
- [18] R. v. Mises, "Mechanik der festen körper im plastisch-deformablen zustand," *Nachrichten von der Gesellschaft der Wissenschaften zu Göttingen, Mathematisch-Physikalische Klasse*, vol. 1913, pp. 582–592, 1913. ↑ 3
- [19] R. Hill, "The mathematical theory of plasticity: Oxford University," *Press New York*, 1950. ↑ 3
- [20] I. J. Levinson, *Mechanics of materials*. Prentice-Hall, 1963. ↑ 3
- [21] P. D. Barsanescu and A. M. Comanici, "von Mises hypothesis revised," *Acta Mechanica*, vol. 228, no. 2, pp. 433–446, 2017. <https://doi.org/10.1007/s00707-016-1706-2>. ↑ 3
- [22] D. Best and N. I. Fisher, "Efficient simulation of the von Mises distribution," *J. R. Stat. Soc., C: Appl. Stat.*, vol. 28, no. 2, pp. 152–157, 1979. <https://doi.org/10.2307/2346732>. ↑ 3
- [23] R. C. Hibbeler, *Mecánica de materiales*. Pearson México, 2017. ↑ 3, 4, 12
- [24] F. P. Beer, E. R. Johnston, J. T. DeWolf, and D. F. Mazurek, *Mecánica de materiales*. McGraw-Hill Education, 2021. ↑ 3, 4, 12

- [25] M. Kamoji, S. B. Kedare, and S. Prabhu, "Experimental investigations on single stage modified Savonius rotor," *Appl. Energy.*, vol. 86, no. 7-8, pp. 1064–1073, 2009. <https://doi.org/10.1016/j.apenergy.2008.09.019>. ↑ 3
- [26] K. S. Jeon, J. I. Jeong, J.-K. Pan, and K.-W. Ryu, "Effects of end plates with various shapes and sizes on helical Savonius wind turbines," *Renew. Energ.*, vol. 79, pp. 167–176, 2015. <https://doi.org/10.1016/j.renene.2014.11.035>. ↑ 3
- [27] S. Roy and U. K. Saha, "Review of experimental investigations into the design, performance and optimization of the Savonius rotor," *Proc. Inst. Mech. Eng. A: J. Power Energy*, vol. 227, no. 4, pp. 528–542, 2013. <https://doi.org/10.1177/0957650913480992>. ↑ 4
- [28] T. Hayashi, Y. Li, and Y. Hara, "Wind tunnel tests on a different phase three-stage Savonius rotor," *JSME Int. J. Ser. B*, vol. 48, no. 1, pp. 9–16, 2005. <https://doi.org/10.1299/jsmeb.48.9>. ↑ 4
- [29] M. Braza, A. Bottaro, and M. Thompson, "Advances in fluid-structure interaction," 2016. ↑ 4
- [30] Y. Bazilevs, K. Takizawa, and T. E. Tezduyar, *Computational fluid-structure interaction: Methods and applications*. John Wiley & Sons, 2013. ↑ 4
- [31] J.-F. Sigrist, *Fluid-structure interaction: An introduction to finite element coupling*. John Wiley & Sons, 2015. ↑ 4
- [32] H.-J. Bungartz, M. Mehl, and M. Schäfer, *Fluid Structure Interaction II: Modelling, Simulation, Optimization*, vol. 73. Springer Science & Business Media, 2010. ↑ 4
- [33] F. Axisa and J. Antunes, *Modelling of mechanical systems: Fluid-structure interaction*, vol. 3. Elsevier, 2006. ↑ 4
- [34] G. P. Galdi and R. Rannacher, *Fundamental trends in fluid-structure interaction*, vol. 1. World Scientific, 2010. ↑ 4
- [35] G. Hou, J. Wang, and A. Layton, "Numerical methods for fluid-structure interaction: A review," *Commun. Comput. Phys.*, vol. 12, no. 2, pp. 337–377, 2012. <https://doi.org/10.4208/cicp.291210.290411s>. ↑ 5
- [36] S. Bhakade, S. Kumbhar, Y. Mohite, and P. Kengar, "A review on fluid structure interaction analysis methodology," *Int. j. trend res. dev.*, vol. 3, no. 3, pp. 617–6199, 2016. ↑ 5
- [37] T. Belytschko, "Fluid-structure interaction," *Comput. Struct.*, vol. 12, no. 4, pp. 459–469, 1980. [https://doi.org/10.1016/0045-7949\(80\)90121-2](https://doi.org/10.1016/0045-7949(80)90121-2). ↑ 5
- [38] J. Penrose, D. Hose, C. Staples, I. Hamill, I. Jones, and D. Sweeney, "Fluid structure interactions: Coupling of cfd and fe," in *18th CAD-FEM User's Meeting-International Congress on FEM Technology*, 2000. ↑ 5
- [39] K. Molina, D. Ortega, M. Martínez, W. Pinto-Hernández, and O. A. G. Estrada, "Modelado de la interacción fluido estructura (fsi) para el diseño de una turbina eólica hawt," *Revista UIS Ingenierías*, 2018. <https://doi.org/10.18273/revuin.v17n2-2018023>. ↑ 5
- [40] A. Beckert, "Coupling fluid (cfd) and structural (fe) models using finite interpolation elements," *Aerosp. Sci. Technol.*, vol. 4, no. 1, pp. 13–22, 2000. [https://doi.org/10.1016/S1270-9638\(00\)00111-5](https://doi.org/10.1016/S1270-9638(00)00111-5). ↑ 5

-
- [41] Y. L. Young, "Fluid-structure interaction analysis of flexible composite marine propellers," *J. Fluids Struct.*, vol. 24, no. 6, pp. 799–818, 2008. <https://doi.org/10.1016/j.jfluidstructs.2007.12.010>. ↑ 5
- [42] B. Andersson, R. Andersson, L. Håkansson, M. Mortensen, R. Sudiyo, and B. Van Wachem, *Computational fluid dynamics for engineers*. Cambridge university press, 2011. ↑ 5, 8
- [43] F. R. Menter, M. Kuntz, and R. Langtry, *Ten years of industrial experience with the SST turbulence model*, vol. 4. 2003. ↑ 5
- [44] N. Alom and U. K. Saha, "Influence of blade profiles on Savonius rotor performance: Numerical simulation and experimental validation," *Energy Convers. Manag.*, vol. 186, pp. 267–277, 2019. <https://doi.org/10.1016/j.enconman.2019.02.058>. ↑ 5
- [45] P. Jain, *Wind energy engineering*, New York: McGraw-Hill Education, 2016. ↑ 5
- [46] H. K. Versteeg and W. Malalasekera, *An introduction to computational fluid dynamics: The finite volume method*. Pearson education, 2007. ↑ 5
- [47] S. Mathew, *Wind energy: fundamentals, resource analysis and economics*, vol. 1. Springer, 2006. <https://doi.org/10.1007/3-540-30906-3>. ↑ 6
- [48] M. Al-Ghriyah, M. F. Zulkafli, D. H. Didane, and S. Mohd, "The effect of inner blade position on the performance of the savonius rotor," *Sustain. Energy Technol. Assess.*, vol. 36, p. 100534, 2019. <https://doi.org/10.1016/j.seta.2019.100534>. ↑ 6
- [49] I. Ross and A. Altman, "Wind tunnel blockage corrections: Review and application to Savonius vertical-axis wind turbines," *J. Wind. Eng. Ind. Aerodyn.*, vol. 99, no. 5, pp. 523–538, 2011. <https://doi.org/10.1016/j.jweia.2011.02.002>. ↑ 6
- [50] S. Roy and U. K. Saha, "An adapted blockage factor correlation approach in wind tunnel experiments of a Savonius-style wind turbine," *Energy Convers. Manag.*, vol. 86, pp. 418–427, 2014. <https://doi.org/10.1016/j.enconman.2014.05.039>. ↑ 6
- [51] K. Almohammadi, D. Ingham, L. Ma, and M. Pourkashan, "Computational fluid dynamics (cfd) mesh independency techniques for a straight blade vertical axis wind turbine," *Energy*, vol. 58, pp. 483–493. <https://doi.org/10.1016/j.energy.2013.06.012>, 2013. ↑ 8
-

Luis Antonio Gallo Jaramillo

Master of Mechanical Engineering from Universidad de Antioquia; Mechanical Engineer from the same university. He is part of the Research Group on Alternative Energy (GEA) at Universidad de Antioquia. Professor at the Universidad de Pamplona.

Email: luis.gallo@udea.edu.co

Edwin Lenin Chica Arrieta

PhD in Engineering from the University of Valladolid (Spain). Master of Engineering and Specialist in Mechanical Design from Universidad Eafit (Colombia). Mechanical Engineer from Universidad de

Antioquia (Colombia). Professor at Universidad de Antioquia and leader of the Research Group on Alternative Energy (GEA) from the same university.

Email: edwin.chica@udea.edu.co

Elkin Gregorio Flórez Serrano

PhD in Mechanical Engineering from the Polytechnical University of Catalonia in Barcelona (Spain). Master of Mechanical Engineering from Universidad de los Andes (Colombia) and Master of Chemical and Process Engineering from Rovira i Virgili University, Tarragona campus (Spain). Mechanical Engineer from Universidad Francisco de Paula Santander, Cúcuta campus. Tenured professor of the Mechanical Engineering program at the University of Pamplona. Director of the Research Group in Mechanical Engineering at the University of Pamplona (GIMUP).

Email: eflorez@unipamplona.edu.co

